
Princeton Plasma Physics Laboratory

PPPL-

PPPL-



Prepared for the U.S. Department of Energy under Contract DE-AC02-09CH11466.

Princeton Plasma Physics Laboratory

Report Disclaimers

Full Legal Disclaimer

This report was prepared as an account of work sponsored by an agency of the United States Government. Neither the United States Government nor any agency thereof, nor any of their employees, nor any of their contractors, subcontractors or their employees, makes any warranty, express or implied, or assumes any legal liability or responsibility for the accuracy, completeness, or any third party's use or the results of such use of any information, apparatus, product, or process disclosed, or represents that its use would not infringe privately owned rights. Reference herein to any specific commercial product, process, or service by trade name, trademark, manufacturer, or otherwise, does not necessarily constitute or imply its endorsement, recommendation, or favoring by the United States Government or any agency thereof or its contractors or subcontractors. The views and opinions of authors expressed herein do not necessarily state or reflect those of the United States Government or any agency thereof.

Trademark Disclaimer

Reference herein to any specific commercial product, process, or service by trade name, trademark, manufacturer, or otherwise, does not necessarily constitute or imply its endorsement, recommendation, or favoring by the United States Government or any agency thereof or its contractors or subcontractors.

PPPL Report Availability

Princeton Plasma Physics Laboratory:

<http://www.pppl.gov/techreports.cfm>

Office of Scientific and Technical Information (OSTI):

<http://www.osti.gov/bridge>

Related Links:

[U.S. Department of Energy](#)

[Office of Scientific and Technical Information](#)

[Fusion Links](#)

The physics basis for a conservative physics and conservative technology tokamak power plant, ARIES-ACT2

C. E. Kessel¹ and F. M. Poli¹

¹Princeton Plasma Physics Laboratory

Abstract

The conservative physics and conservative technology tokamak power plant ARIES-ACT2 has a major radius of 9.75 m at aspect ratio of 4.0, strong shaping with elongation of 2.2 and triangularity of 0.63. The no wall β_N reaches ~ 2.4 , limited by $n=1$ external kink mode, and can be extended to 3.2 with a stabilizing shell behind the ring structure shield. The bootstrap current fraction is 77% with a q_{95} of 8.0, requiring about ~ 4.0 MA of external current drive. This current is supplied with 30 MW of ICRF/FW and 80 MW of negative ion NB. Up to 1.0 MA can be driven with LH with no wall, and 1.5 or more MA can be driven with a stabilizing shell. EC was examined and is most effective for safety factor control over $\rho \sim 0.2-0.6$ with 20 MW. The pedestal density is $\sim 0.65 \times 10^{20} / \text{m}^3$ and the temperature is ~ 9.0 keV. The H_{98} factor is 1.25, $n/n_{Gr} = 1.3$, and the net power to LH threshold power is 1.3-1.4 in the flattop. Due to the high toroidal field and high central temperature the cyclotron radiation loss was found to be high depending on the first wall reflectivity.

I. Introduction

The tokamak power plant study described here is to represent a conservative physics and conservative technology configuration, as part of the ARIES-ACT (advanced conservative tokamak) four corners study¹. The previous study, ARIES-ACT1² examined an advanced physics and advanced technology example. The strong plasma shaping with $\kappa_x = 2.2$ and $\delta_x = 0.625$, and up-down symmetric double null, is preserved to provide robust stability limits and large operating space for solutions. The aspect ratio is taken to be 4.0, since previous studies³⁻⁵ have shown weak sensitivity to this parameter in the range of 3.0-5.0. This technology solution utilizes the Dual Coolant Lead Lithium blanket design⁶ and He-cooled tungsten divertor⁷. This plant has a thermal conversion efficiency of $\sim 44\%$, but otherwise has the same auxiliary systems power requirement (32 MW), same heating and current drive wall-plug efficiency (0.4), and approximately same fraction of gross thermal power required for pumping ($\sim 1\%$). An additional technology constraint on this configuration is that the peak heat flux in the divertor not exceed $10 \text{ MW}/\text{m}^2$. The plasma is constrained to be below the no wall beta limit, have a global energy confinement multiplier (IPB98y2)⁸ less than 1.3, and a ratio of density to Greenwald density below 1.3. It is found that the $\beta_N^{\text{no-wall}}$ is approximately 2.4, and is sensitive to current near the plasma edge. Higher values can be tolerated, $\beta_N \sim 2.9-3.2$, with a conducting structure behind the structural ring and shield, and would require rotation, feedback coils, and/or kinetic stabilization⁹⁻¹³. Systems analysis (0-dimensional) has been performed to identify an attractive operating point within these constraints, and 1.5D time-dependent free-boundary simulations have been executed to target these plasma parameters. A range of temperature profiles are generated, in combination with a single density profile assumption, to provide plasma profiles with varied peakedness.

Heating and current drive was analyzed for ion cyclotron radio-frequency (ICRF), negative ion neutral beams (NB), electron cyclotron (EC), and lower hybrid (LH). Peeling-ballooning calculations with EPED1¹⁴ showed that the pedestal for this plasma would be ~ 220 kPa at a pedestal density of $0.8 \times 10^{20} / \text{m}^3$, which for the densities at the pedestal in the 1.5D simulations of $\sim 0.65 \times 10^{20} / \text{m}^3$ results in pedestal temperatures of ~ 8.8 - 9.2 keV. The resulting configuration at high toroidal field and low plasma density resulted in good LH accessibility, allowing the waves to penetrate and damp at normalized minor radii of $\rho = 0.65$ - 0.8 .

II. Systems Analysis Identification of the Operating Point

The systems code¹⁵ utilized by the project solves for a 0D plasma power and particle balance, including plasma radiation, and current drive and bootstrap current, along with a series of engineering assessments (first wall and divertor heat flux, neutronic build, TF coil, PF coil, thermal conversion and plant power balance) to determine an operating point's viability. Ultimately the power plant configuration is constructed around the plasma and its cost is determined. The method used is a database approach, where several parameters are scanned to produce a large database of physics configurations, which are subsequently analyzed through the engineering and inboard radial build assessments¹. For the conservative plasma configurations the β_N is scanned from 2.0 to 4.0%, plasma gain Q from 12.5 to 40, toroidal field from 5.5 to 10.5 T, q_{95} from 3.5 to 9.0, n/n_{Gr} from 0.8 to 1.6, argon impurity fraction from 0.2 to 0.3%, and major radius from 5.0 to 11.0 m. The density profile peak to volume average is scanned from 1.25-1.4, and temperature peak to volume average at 2.15-3.0. Fixed parameters in the systems scan are plasma aspect ratio at 4.0, triangularity at 0.575, elongation at 2.1 (shape parameters at actual free-boundary separatrix are 0.625 and 2.2, respectively), τ_p^* / τ_E of 5.0, current drive (CD) efficiency in the plasma of 0.15 MA/m²-MW. Since the best current drive sources for the low beta plasma were not known a priori, a low CD efficiency was assumed. These scan ranges and fixed parameters are determined by initially running several scoping evaluations with the systems code. A large number of viable physics operating points are established that satisfy the balance equations. These points are then run through the engineering module, the power core is built around the plasma, cost determined and filtered to provide 1000 MW electric power operating points. The filters used, in addition to 1000 MW electric, were $n/n_{Gr} \leq 1.3$, $\beta_N^{th} + \beta_N^{fast} \leq 2.65$, $H_{98} \leq 1.3$, and $q_{div}^{peak} \leq 10$ MW/m². In this case the cost of electricity was not used significantly in ordering the operating points. Instead, other criteria were examined, including maximizing fusion gain, maintaining the peak toroidal field at the toroidal field coil less than 16 T¹⁶, and minimizing major radius, since these plasmas were ending up at large major radii and high toroidal fields at the plasma.

The temperature and density profiles in the systems analysis are given by, where ρ is a normalized minor radius (r/a),

$$n(\rho) = n(0)[(1 - f_n)(1 - \rho^2)^{\alpha_n} + f_n]$$

$$T(\rho) = T(0)[(1 - f_T)(1 - \rho^2)^{\alpha_T} + f_T]$$

Since the systems analysis does not represent the plasma as accurately as a 1.5D analysis, it is necessary to establish input parameters to the systems code that will properly reproduce those from a 1.5D analysis. The exponents and the edge values are adjusted to provide this agreement by comparisons with actual values of central, peak to volume average and edge parameter values. In addition, the plasma volumes are made to agree by using shape parameters at a flux surface slightly less than the separatrix values (e.g. 2.1 for elongation rather than the actual separatrix value of 2.2). Table I shows several parameters from the systems code reference operating point, and 6 cases generated in 1.5D time-dependent analysis with different energy transport assumptions combined with prescribed density magnitude and profile shape.

III. Time-dependent 1.5D Simulations

The Tokamak Simulation Code (TSC)¹⁷ is a predictive plasma evolution code, solving the free-boundary 2-D axisymmetric MHD Maxwell's equations on a rectangular grid. 1D surface averaged transport equations are solved for energy, utilizing a modified Coppi-Tang^{18,19} transport model with a prescribed pedestal and profile peakedness. The density profile is prescribed with a peak to volume average of 1.4-1.5²⁰, with a pedestal feature and finite separatrix value at 0.35 times the central value, $n(0)$. The discharge parameters are transferred to TRANSP²¹, to access high fidelity heating and current drive analysis, discussed in Section 4. The TSC is used to simulate the time-dependent evolution of the ARIES-ACT2 plasma from early startup ($I_p = 500$ kA) to relaxation of the profiles (typically > 2500 s). Six cases are examined, with varying temperature profiles, and one density profile. These are described by 1) broad pressure, 2) broad pressure with flattened center, 3) medium peaking pressure, 4) medium peaking pressure with flattened center, 5) peaked pressure, and 6) peaked pressure with flattened center. The plasma begins as a full bore plasma, limited on the inboard wall, at a plasma current of 500 kA, and is grown (primarily vertically) to full size and shape over the course of 100-150 s. The plasma magnetic divertor X-point forms very early in order to isolate the plasma from the wall and allow the injection of heating and current drive power. Fig. 1 shows a fully relaxed flattop plasma configuration for the broad pressure case, showing the primary toroidally continuous conducting structures, which are comprised of the tungsten stabilizer plates, the steel ring structure, internal vertical position feedback coils, and the steel vacuum vessel, in order beginning from closest to the plasma, described in more detail in Ref 22. The poloidal field coils will be discussed in section V. Figs. 2 shows the plasma profiles for current density, input power and radiation losses. Fig. 3 and 4 show time histories of plasma current contributions and powers, density, internal inductance, global energy confinement multiplier (H_{98}), β_N , and L-H threshold and net powers. These are for the broad pressure configuration, and are typical of all the cases presented here. Parameters for all 6 cases are given in Table I, and profiles for them are shown in Fig. 5. It is found that the plasma requires ~ 320 V-s to reach full current at 14 MA, and this includes resistive, internal and external inductive contributions. Here it is assumed that 20 V-s are used to bring the plasma to 0.5 MA, giving a total swing of -120 to + 200 Wb. The thermal diffusivity is adjusted through an exponent to provide the

peakedness in the temperature profile. In the flattening cases, a modification is used in the core to increase transport and provide a weaker temperature gradient. These diffusivities are globally adjusted to provide sufficient global confinement to reach the desired β level, identified by the systems analysis. The top of the pedestal pressure height is determined by the peeling ballooning model EPED1¹⁴ to be approximately 185 kPa, giving $T_{\text{ped}} \sim 9$ keV, where we refer to the top of the pedestal. In all cases argon is introduced as the core plasma line radiating impurity at 0.3% of the electron density.

Table I. Plasma Parameters from Systems Analysis Reference and 1.5D Simulations

	Sys Op Point	broad p	broad p flattening	medium p	medium p flattening	peaked p	peaked p flattening
I_p , MA	13.98	14.0	14.0	14.0	14.0	14.0	14.0
I_{BS} , MA	10.8	10.2	10.4	10.5	11.1	10.6	10.6
I_{IC} , MA	3.2	0.70	0.70	0.70	0.70	0.70	0.70
I_{NB} , MA		2.97	3.05	2.83	2.65	2.70	2.87
$q_{\text{min}}, q(0)$		1.22, 1.22	1.73, 1.73	1.20, 1.20	1.60, 1.60	1.06, 1.06	1.26, 1.26
l_i	0.75 (input)	0.78	0.73	0.82	0.74	0.88	0.75
n/n_{Gr}	1.3	1.21	1.23	1.29	1.33	1.36	1.23
W_{th} , MJ	1486	1532	1563	1586	1650	1596	1650
$n(0)$, /m ³ $\times 10^{20}$	1.25	1.15	1.15	1.25	1.25	1.30	1.15
$\langle n \rangle_v$, /m ³ $\times 10^{20}$	0.86	0.76	0.77	0.81	0.84	0.825	0.82
$n(0)/\langle n \rangle$	1.45	1.5	1.5	1.53	1.49	1.56	1.40
$\beta_N^{\text{th}}, \beta_N^{\text{total}}$	2.25, 2.60	2.4, 2.75	2.42, 2.77	2.45, 2.80	2.57, 2.92	2.50, 2.85	2.70, 3.05
τ_{E_s} , s	3.99	4.33	4.10	4.22	4.00	4.29	4.57
$H_{98(v,2)}$	1.22	1.29	1.26	1.25	1.29	1.25	1.37
$T_{e,i}(0)$, keV	38.3	42.9	35.6	44.1	36.8	46.4	40.4
$T(0)/\langle T \rangle$	2.15	2.28	1.95	2.43	2.03	2.65	2.13
P_{α} , MW	528	493	514	533	574	550	538
P_{IC} , MW	105.5	30	30	30	30	30	25
P_{NB} , MW		80	80	80	80	80	75
P_{cycl} , MW	150.4	133.0*	128.6*	133.3*	133.3*	135.7*	142.3*
P_{line} , MW	42.9	40.0	42.9	48.2	51.8	53.6	46.2
P_{brem} , MW	96.5	67.0	67.9	74.0	74.0	75.0	69.2
$P_{L-H,\text{thr}}$, MW	268	264	270	285	284	290	274
$P_{\text{net}}/P_{L-H,\text{thr}}$	1.28	1.38	1.43	1.37	1.48	1.34	1.37
Z_{eff}	2.12	2.06	2.06	2.06	2.06	2.06	2.06
n_{He}/n_e	0.097	0.092	0.097	0.105	0.105	0.100	0.104
n_{DT}/n_e	0.750	0.753	0.757	0.752	0.740	0.750	0.754
n_{Ar}/n_e	0.003	0.003	0.003	0.003	0.003	0.003	0.003

*assuming first wall reflectivity of 90%.

All the 1.5D cases ended up at slightly higher β_N values than the target from the 0D analysis, and are also above the no wall β_N determined by ideal MHD analysis. They can be stabilized with a faraway wall behind the structural ring which is discussed in Sec IV. The plasma internal self-inductance, l_i , ranges from 0.73-0.88. The central temperatures were in the range of 35-46 keV, and density peak to volume average values

ranged from 1.4-1.56. The standoff of the flattop burn plasma net power ($P_{\text{net}} = P_{\text{alpha}} + P_{\text{input}} - P_{\text{rad}} - dW/dt$) to the L to H threshold power²³, was only 1.37-1.48, and using only a fraction of the line radiation (outside the pedestal, for example) would not change this number significantly. The peak density values are $1.15\text{-}1.30 \times 10^{20} / \text{m}^3$ and the volume average values are $0.76\text{ to }0.84 \times 10^{20} / \text{m}^3$. The central safety factors are all above 1.0, with the peaked pressure case getting very close to 1.0, and the flattened broad pressure case having the highest at 1.73. These all turned out to be monotonic q-profiles, however, there are sensitivities to the ICRF FWCD profile that can lead to very localized reverse shear near the magnetic axis.

With the large toroidal field and high electron central temperatures, the cyclotron radiation loss is significant, amounting to ~ 130 MW with a 90% reflectivity assumed for the first wall. Simulations assuming 60%, 75% and 90% for this reflectivity showed that the cyclotron power loss went from 196 to 167, and to 125 MW, respectively. In those simulations this trend was compensated by raising the density since this reduces the temperature while raising the fusion heating source. It would also be possible to reduce the argon concentration and correspondingly the line radiation. Since the reflectivity of surfaces is highly uncertain²⁴, the actual power loss is difficult to estimate, although tracking the cyclotron loss is important to knowing the electron power balance in the plasma. Assuming very high first wall reflectivity makes it difficult to know when it is increasing. The systems analysis assumes a default value of 60% so that increased radiation can be seen in operating space scans.

In the rampup phase of the time-dependent simulations, it was found that driving current with NB and IC sources was difficult. The NB shins thru restricted its use until nearly the end of the current rampup phase, and the ICRF FW was not efficient enough to drive significant levels of current. Inductive current was driven by the solenoid and poloidal field coils to compensate, requiring ~ 300 V-s to bring the plasma to flattop, and the resulting inductive current decays slowly over approximately 1000-2000 s. The inductive current diffuses to the plasma center where the temperature is high and the current diffusion time is long. The use of LHCD or EC can aid in driving current during the rampup, reducing the amount of inductive current driven, and heating electrons in order to reduce resistive V-s consumption. Simulations using the LH in the ramp phase showed that heating was effective, while the current drive was weak due to too low an n_{\parallel} (since it is determined by the flattop plasma parameters) for driving current, leading to a reduction of the V-s requirement to reach the beginning of plasma current flattop, but otherwise not displacing a significant amount of inductive current. This remains an issue for further examination.

IV. Ideal MHD stability of low-n external kink, high-n ballooning modes, vertical mode, and peeling-ballooning modes

The plasma configurations established by the time-dependent TSC simulations are examined for their ideal MHD stability to low-n external kink modes, high-n ballooning modes. The PEST1²⁵ code is used for the low-n and the BALMSC²⁶ code is used for the

high- n modes. The JSOLVER²⁷ fixed boundary flux-coordinate equilibrium solver is used to recalculate and refine the equilibrium before mapping for stability calculations. The plasma characteristics are input to the EPED1¹⁴ peeling-ballooning analysis to determine the pedestal pressure height expected, giving a total pedestal pressure of 220 kPa at a pedestal density of $0.8 \times 10^{20} / \text{m}^3$, which scaled to the reference density of $0.65 \times 10^{20} / \text{m}^3$ gives about 185 kPa. There is a trend to higher pedestals at higher density since the higher collisionality reduces the local bootstrap current and the drive for peeling instabilities. The location of the top of the pedestal is determined to be at a poloidal flux of 0.89. Here we assume that the ion density and temperatures are the same as the electrons at the pedestal. This pedestal pressure range is enforced for all time-dependent and stability analyses.

Initial low- n kink studies, done before 1.5D plasma analysis to guide systems analysis, were used to determine the range of stable β_N in the absence of a stabilizing wall, and how a far away wall might improve this. This was first done with parameterized current density and pressure profiles in the JSOLVER code,

$$p = p_o [(1 - f_{ped})(1 - x^b)^a + f_{ped} \tanh(\rho_{ped}, \Delta_{ped})]$$

$$j_{||} = j_{||o} [c_1(1 - x^{b1})^{a1} + (1 - c_1)(1 - x^{b2})^{a2}]$$

which are varied independently, making the current and pressure profiles broad or peaked. Fig. 6 shows the boundary of stability for the $n=1$ external kink mode in the absence of a stabilizing wall, with black X's. This shows the higher stable β_N as l_i increases, although this is typically constrained by the presence of an H-mode pedestal that limits how high l_i can get. The dashed line is to show the upper bound observed from these calculations. The next examination used an algorithm in JSOLVER that determines the bootstrap current consistently with the pressure, density, and q profiles, superimposed with model CD sources for ICRF/FWCD, NBCD, LHCD and ECCD, providing 100% non-inductive current density. It was found that introducing LHCD in the outer 20% of the minor radius tended to reduce the stable β_N with no stabilizing shell. In the absence of LHCD, combinations of ICRF/FWCD and ECCD, ICRF/FWCD and NBCD, or just NBCD could give stable plasmas at around β_N - l_i of 2.6-0.78, which is shown in Fig. 6 as a blue circle. Also in the absence of LHCD, the β_N could be increased to 2.85 and 3.18, which subsequently lowers l_i , by assuming a stabilizing wall at 0.675a and 0.45a, respectively, measured from the plasma boundary. These walls would lie roughly behind the structural ring/shield, and breeding blanket, respectively. These are shown by the two orange open circles. If there are sufficiently continuous structural shells in these locations, they may serve as stabilizing shells. On present experimental tokamaks, the vacuum vessel, which is relatively close to the plasma, serves as a stabilizing shell for external kink modes, and must be included to get consistency with ideal MHD predictions. Overall, the low- n ideal MHD stability was quite sensitive to current driven in the outer regions of the plasma, both by an external source like LH or by the pedestal bootstrap current. This provided the basis for the systems analysis filtering of the operating points to keep $\beta_N^{\text{total}} < 2.65$.

Finally, the relaxed configurations derived from the 1.5D plasma simulations were examined for their ideal MHD stability, which includes the enforcement of the EPED1 pedestal prediction. All cases were found to be high-n ballooning stable. The pedestal resulted in reduced beta limits, and it was directly influencing the global low-n stability. The no stabilizing wall cases analyzed are shown in Fig. 6 (as red circles), showing that maximum β_N levels are closer to 2.35-2.45. JSOLVER is used to reduce the pressure from the 1.5D equilibria and recalculate the equilibrium for these cases. In addition, due to the deeper penetration of LH at the ACT2 parameters, using 0.5-1.0 MA of LHCD did not change the beta limits as earlier estimated, since it is not localized to the plasma edge as was assumed. Using LHCD at a level of 1.5 MA did begin to reduce the beta limit in the absence of a stabilizing wall, and these points lie at the low β_N and low l_i region of Fig. 8 (red circles). In these cases with LH we are reducing the FWCD and NBCD by a corresponding level of MA, and the total input power is changed by +/-10% at the most. Therefore LHCD could be used to offset the FWCD and NBCD, resulting in higher $q(0)$ and higher bootstrap current.

In the final design of the ACT2 power plant, on the outboard side, the back of the breeding region of the blanket lies at 1.15 m from the plasma surface, or a normalized wall location of $b/a = 0.47$. The back of the structural ring and shield lies at 1.35 m, or $b/a = 0.55$. If sufficient conducting structure exists in these locations, it is found that both the beta limit and the tolerance for LHCD can be substantially increased. The JSOLVER equilibrium code was used to raise the plasma pressure in the 1.5D derived equilibria, both with and without LHCD, which is not entirely self-consistent with the 1.5D solutions, but sufficient for scoping. Shown in Fig. 8 by the green points are plasmas with β_N values between 2.85-3.25, some with LH of 0.5 to 1.5 MA, and others without LH, stabilized with a conducting shell behind the structural ring and shield ($b/a = 0.55$). The trend for the with wall cases show higher β_N with lower l_i , due to the stronger coupling of broad current profile to the far away wall. A structural shell at this location would not interfere with tritium breeding, as it does in the high β_N configurations like ACT1. The stabilization of resistive wall modes would require plasma rotation, feedback, and/or kinetic stabilization in addition to the conducting shell. The structures, which could be ferritic steel or a dedicated structure made of tungsten, are located over the outboard region and are not toroidally continuous. The thickness of this shell is chosen to provide a time constant ($\tau_w \sim \mu_0 \Delta b / \eta_w$) of about 0.1 s, to allow for reasonable feedback currents and voltages^{9,10} ending up about 1 cm thick for tungsten, or ~ 6 cm thick for ferritic steel. Normal copper feedback coils for the resistive wall mode, the mode that the external kink mode becomes in the presence of a resistive shell, are located behind the blanket and shield, and are individual window coils on each sector (16 in total).

There are vertical position feedback coils located behind the shield, above and below the midplane, which are normal copper coils, and can be seen in Fig. 1. These work in conjunction with the dedicated tungsten stabilizing shells located both on the outboard, approximately from 60-90 degrees from plasma geometric center, and the inboard. From previous work on stabilizing shell locations²⁸ for vertical stability, the plasma elongation of 2.2 requires a shell on the outboard at about 0.33 times the plasma minor radius,

measured from the plasma boundary, which is 80 cm from the plasma. This achieves a stability factor, $1 + \tau_g/\tau_{L/R}$, of 1.2, which corresponds to a safe resistive wall location. The ratio of conductor shell thickness to resistivity Δ/η for vertical stability is approximately determined to be $\sim 1.0 \times 10^5$ /ohm, for feedback coils located behind the shield, toroidally continuous shells, and proper poloidal coverage noted above. The shells are a few cm thick, and will be made toroidally continuous by having them traverse radially outward to the back of the shield or ring structure where connections are made. Tungsten is chosen to provide high electrical conductivity along with high temperature operation typical of the blanket.

V. Poloidal Field Coil Design

The poloidal field (PF) coils must provide the plasma equilibrium force balance and assist in driving inductive current in the current rampup phase. The inboard solenoid coils primarily provide the inductive current drive and the outer PF coils primarily provide the equilibrium, although strictly speaking each coil contributes to both functions. The plasma is found to require ~ 300 V-s of assistance in ramping up the plasma current from 500 kA to 14 MA, with an additional 20 V-s assumed to be lost in breakdown and early startup phases before reaching $I_p = 500$ kA. Both equilibrium calculations and TSC are used to establish fiducial states where the coil currents are examined in order to determine the best location for the coils. These fiducial states span plasma current from 500 kA to the flattop value of 14 MA, $l_i(1)$ values from 1.3 to 0.7, β_N values of 0 to 2.75, and flux states from -120 to +200 Wb. The coil locations, sizes, and maximum coil currents obtained anywhere in the rampup or flattop are shown in Table II. The coil locations are significantly constrained in terms of their closeness to the plasma by the radial build from first wall, breeding blanket, shield and support, vacuum vessel, TF coil, and TF coil support structures. In addition, the coils are limited in poloidal distribution by supports, manifolding and ductwork. The radial maintenance scheme employed on ARIES power plants precludes coils on the outboard side. Shown in Fig. 7 is the flattop plasma boundary and final poloidal field coil distribution. The coil cross-sections are also listed in Table II, and are determined with an assumed maximum overall coil current density of 15 MA/m².

Table II. ARIES-ACT2 poloidal field coil parameters.

	R, m	Z, m	ΔR , m	ΔZ , m	$ I_{max} $, MA
CS1	4.22	1.30	0.4	4x0.65	1.30
CS2	4.22	3.90	0.4	4x0.65	3.88
PF1	4.98	10.42	0.585	0.585	5.14
PF2	6.20	10.57	0.539	0.539	4.35
PF3	7.36	10.85	0.596	0.596	5.32
PF4	10.47	11.02	0.925	0.925	12.82
PF5	13.72	10.38	0.486	0.486	3.54
PF6	15.24	9.87	0.658	0.658	6.50
PF7	16.61	9.25	1.036	1.036	16.10

VI. Heating and Current Drive Systems

The time-dependent simulations of the plasma configurations utilize negative ion neutral beam (NB) and ion cyclotron radio-frequency (ICRF) heating and current drive (H/CD). These are examined in terms of steering, particle energy, frequency, and power, to determine the best parameters for the power plant configuration. The systems code identifies heating and current drive powers separately, so they do not have to be equal, but are typically very close. The 1.5D analysis determines actual efficiencies for the current drive. Electron cyclotron (EC) H/CD is also examined to provide on-axis and near-axis current drive flexibility to manipulate the q-profile. Although lower hybrid (LH) current drive was assumed to place current in the edge plasma where the no-wall ideal stability would be negatively affected, it was found from detailed analysis to penetrate the plasma to ρ of 0.65, had a broad deposition profile, and ultimately it did not negatively affect the ideal MHD stability, so long the magnitude of the driven current remained below at or below ~ 1.0 MA. The use of LH was examined as a means to reduce the near axis current drive and raise $q(0)$, which tends to increase the bootstrap current, providing some flexibility in the plasma configuration.

ICRF is used to heat ions, and electrons, and also drive on-axis current with a relatively narrow distribution when phased to do so. This function is useful for providing a seed current on axis that avoids high values of the on-axis safety factor. For the toroidal field of 8.75 T at the plasma major radius (9.75 m), the frequency range of 45-110 MHz was examined to understand the damping between thermal and fast fuel ions, impurities, and electrons, as well as current drive. The primary focus was the 2nd tritium resonance ($2\omega_{cT}$) near the geometric center or slightly on the high field side, while avoiding other fuel, thermal helium, fast alpha particle, or impurity resonances. The plasma species are taken to be D, T, thermal He, fast helium (alpha particles), fast D from NB's, argon, and electrons. The analysis used is the TORIC full wave code^{29,30}, with a toroidal mode number of 30, launched from the outboard midplane. These calculations were performed on the broad pressure with flattening plasma configuration in the TRANSP code with a Fokker Planck treatment of the resonant ions (tritium) and equivalent Maxwellians for the fast alphas and fast NB deuterons. The electron channel damping provides current drive and so the frequencies with high electron heating fraction are preferred. In addition to the 2nd harmonic of tritium, the frequencies around the fundamentals of D and T were examined since ion damping should be weaker there, although complicated by the various species present. In steady state the optimum frequency appears around 95 MHz, where the wave power was absorbed on thermal tritium, amounting to 63%, and 37% on electrons. There is no alpha particle, thermal or fast deuterium absorption, or argon absorption. The 95 MHz also provided a high CD efficiency of 0.023 A/W, or (nRI/P) 0.26 A/W-m², driving 0.7 MA with 30 MW of power to the plasma, and is the reference for ARIES-ACT2. Shown in Fig. 8 are the absorbed power fractions on electrons, thermal ions, and fast deuterium and alpha particles over the range of ICRF frequencies of 45-110 MHz. The frequency range around the 2nd deuterium resonance is avoided due the combined thermal deuterium, fast deuterium, and fast alpha absorption, in spite of the fact that the electron heating is about the same as that near the 2nd tritium harmonic. The plots show that in the low frequency range, near 47 MHz, the electron power absorption

fraction can reach 67%, subsequently driving 1.2 MA, however this is found to be very narrow, bounded by a strong argon and tritium absorption on either side of this frequency. The lower electron absorption fraction, compared to ARIES-ACT1², is attributed to the lower β_e in these configurations, as the damping is proportional to this quantity. Shown in Fig. 9 is the power deposition split between ions and electrons as a function of time, and the profiles for power to thermal electrons, thermal ions, and driven current. Contrary to the ARIES-ACT1 configuration, the full ICRF power is used throughout the flattop phase since the on-axis current is required. This level might be adjusted for feedback in conjunction with the NBCD driven in the same vicinity. In the startup phase 100% of the ICRF power damps on ions until the plasma temperature rises and some electron damping appears, ultimately reaching the power split described before.

The launching structure is taken to be similar to the ITER ICRF multi-strap launcher³¹, with a maximum power density through the first wall of 10 MW/m². The ICRF system is based on 30 MW maximum power to the plasma and requires 3 m² for the launching structure. With additional mechanical support and cooling structures, the total area reserved for this is 3.75 m².

The use of neutral beams (NB), although common and highly reliable on present tokamak experiments, is typically avoided in power plants due to the complications of access of the drift duct into the fusion power core, neutrons streaming up the drift duct toward the neutralizer and source, and its large source and neutralizer components. Here we will examine the negative ion ITER 1 MeV NB source and layout³² as a guide to understand how the NB can be used to drive current. The NUBEAM³³ Monte Carlo orbit following package will be used to calculate the NB parameters in the plasma. The target is to have the NB drift duct fit between 2 TF coils and only impact one sector (first wall, blanket, structural ring) assembly associated with that sector that fits between the TF coils. This largely forces the tangency radius to be on the high field side of the plasma, and near, but higher than, the R-a (= 7.31 m) location. The beam footprint at the entrance through the first wall is taken as rectangular with 0.6 m x 1.2 m (horizontal x vertical) dimensions. The distance from the first wall crossing back to the source is taken to be ~ 24 m, as in ITER. The beam particle energies examined were 1.0 MeV, 750 keV, and 550 keV. The toroidal beam steering is determined by the access requirements above, while the poloidal steering of the beam was varied by changing the source height from the midplane ($Z = 0$) up to $Z = 4.8$ m above the midplane. Shown in Fig. 10 are a series of current density profiles and power density profiles to electrons and ions for 1 MeV particle energy and tangency radius of 7.75 m, with varying source height above the midplane. Also shown are the shinethru and total driven current for 40 MW of NB power, with varying tangency radius, for the 3 particle energies. The current drive efficiency (nRI/P) was about 0.32-0.37 A/W-m² or 0.033-0.038 A/W. The primary attractiveness of the NB heating and current drive is the broad profile and high current drive efficiency, allowing large current to be driven without locally distorting the q-profile. At the low β of the ACT2 configuration, larger total current, as well as current fraction, must be driven, and the NBCD is useful for providing the majority of this.

The reference for ARIES-ACT2 is 1 MeV with a source elevation of 2.0 m above the midplane, and total power of 80 MW. The precise power requirement can vary depending on the central safety factor and resulting bootstrap current, and so values as low as 65 MW can be feasible. The tangency radius is 7.75 m, for the center of the beam footprint. For 80 MW of injected power, at a minimum, 4 beam openings would be required, each with the 0.6 m x 1.2 m first wall power footprint, and approximately an additional 1.5x to each linear dimension, leading to 0.9 m x 1.8 m x 4 = 6.48 m² area on the first wall. This infers a power density through the first wall of about 28 MW/m², slightly larger than that for ITER with the same footprint of 23 MW/m².

Lower hybrid (LH) is examined for off-axis current drive at levels of 0.5-1.0 MA, since ideal MHD indicated that higher levels tended to lower beta limits with no wall stabilization. The Lower Hybrid Simulation Code (LSC)³⁴ is used to provide a 1D Fokker-Planck ray tracing analysis. The parameters of the ACT2 plasma, high toroidal field and low density, provide good accessibility for the LH waves, with minimum $n_{||}^{acc} \sim 1.4-1.5$, depending on the launched frequency. The $n_{||}$ for minimal mode conversion to the fast wave and high CD is about 2.0. Here we assume 5 GHz to avoid the alpha particle absorption, while keeping the waveguide width reasonable. The waves are found to penetrate the plasma well, reaching normalized minor radii of 0.6-0.65, where electron temperatures are about 15-17 keV, compared to a case like ACT1 where the waves reach a normalized minor radii of 0.8 and damp at electron temperatures of about 10 keV. The $n_{||}$ and launching angle on the outboard side were examined to find the optimum current drive. The forward power lobe is scanned from $n_{||} = 1.85-2.5$, with the negative lobe fixed at -4.0, and the power split of 87% forward and 13% backward is used. This power split is used to provide a factor of 1.6 enhancement to the LSC prediction determined from comparisons with GENRAY/CQL3D 2D Fokker Planck calculations³⁵⁻³⁷. The ITER passive-active multi-junction (PAM) launcher concept^{38,39} is assumed to be the same launcher concept used here, which obtains co- I_p and cntr- I_p power fractions of $\sim 70\%$ and $\sim 30\%$, respectively. Table III shows the driven current for 15 MW of power to the plasma, with $n_{||}$ and outboard poloidal launch angle ($\theta = 0$ is the midplane). These indicate that current drive efficiencies of (nRI/P) 0.27-0.33 A/m²-W, or 0.046 A/W. Shown in Fig. 11 are a series of current profiles from TSC simulations while varying the LH launch parameters, for 15 MW of LH power, and midplane launching. The trend of decreasing current drive efficiency at the lowest $n_{||}$ corresponds to increasing conversion of the slow waves to fast waves, which propagate back to the separatrix and reflect into the plasma with $n_{||}$ upshifts and subsequent damping close to the separatrix (of the fast waves). The trend of decreasing current drive efficiency at larger $n_{||}$ is due to progressively shallower penetration before reaching full absorption, with the associated lower temperatures. The maximum driven current occurs at $n_{||} \sim 2.0$. Launching from above the midplane provides the highest current drive per watt and yields deeper penetration of the LH waves, and broader current distributions. It is advantageous for tritium breeding to move the launching structure off the midplane where the neutron flux is highest, since it would occupy the blanket volume from the first wall back to the rear of the shield. Also shown in Fig. 11 are 2 simulations with the NB, IC, and LH, taking 20 and 40 MW of injected LH power, and 60 and 40 MW of NB injected power, respectively. They are compared with the no LH case, and all are with the broad pressure

configuration. The lower LH power case would not require a stabilizing wall, driving 0.75 MA, while the higher LH power case does require a wall behind the ring structure and shield, driving 1.5 MA.

The launching structure was assumed to be a PAM, with maximum power density of 20 MW/m² through the waveguide assembly. For this, 1-1.5 m² are reserved on the first wall for this function, for the total of 20-30 MW of LH power. An additional area is allocated for mechanical support and cooling structures, to make the total LH footprint 1.45-3.0 m². The details of the waveguide size, spacing, and arrangement⁴⁰, have not been specified, although the envelope provided is considered sufficient.

Table III. Lower hybrid driven current (MA) for 15 MW, 5 GHz, P-coIp = 0.87, P-cntrIp = 0.13, for the broad pressure configuration.

I _{LH} , MA	n = 1.85	n = 2.00	n = 2.12	n = 2.25	n = 2.32	n = 2.50
θ = 0	0.50	0.57	0.55	0.49	0.45	0.41
θ = 45	0.49	0.64	0.59	0.52	0.47	0.43
θ = 60	0.50	0.69	0.63	0.55	0.49	0.43

Electron cyclotron current drive (ECCD) is examined as a means to provide CD in the region of the plasma $0.2 < \rho < 0.6$, for fine-tuning the safety factor profile, and possibly to replace the NBCD in that location. Neither ICRF at low frequency or LH can access this intermediate radial location, while the NBCD profile is broad and spans from the axis to nearly $\rho \sim 1.0$. In addition, EC can propagate through vacuum and therefore it has no plasma coupling constraints that both IC and LH do have. For the higher toroidal field of 8.75 T at the plasma major radius, 260 and 290 GHz are examined to place the EC fundamental resonance on the high field side to minimize trapping effects. Launchers were examined at the outboard midplane $R = 12.3$ m, $Z = 0.0, \pm 1.0$ m, and off-midplane varying from 50° to 80° , measured from the plasma geometric center, at the corresponding first wall locations. The poloidal and toroidal steering angles were then scanned to examine the deposition locations and CD efficiency. It is found for 260 GHz that the highest CD efficiency ranges from ~ 0.012 A/W at $\rho = 0.2$ to 0.018 A/W at $\rho = 0.5-0.6$, and the flexibility in deposition location was found to be extensive. These analyses are done with GENRAY^{35,36} and do not include momentum conserving effects⁴¹ on electron-electron collisions, that may increase the driven current prediction. Shown in Fig. 15 are the A/kW CD efficiencies (color code) and deposition locations (labeled black contours) as a function of the combination of poloidal and toroidal (azimuthal) steering angles. The midplane launchers at $Z = 0, Z = -1.0$ m, $Z = +1.0$ m are shown. Other steering and launching cases at 290 GHz are also examined, showing up to 25% higher current drive efficiency with deposition over similar minor radial locations. The best steering combinations for current drive and deposition flexibility are used in time dependent simulations in TRANSP with TORAY^{42,43} with NB and IC simultaneously. Utilizing a combination of 4 launchers whose deposition spanned $\rho = 0.2-0.6$, it was found that ~ 150 MW was required to drive 1.5 MA, and was not competitive with the NBCD in the same location. Adding only 20 MW of EC at the same deposition locations

was able to move the safety factor profile by ~ 0.5 averaged over the minor radial deposition location.

The launching structures for EC would be smaller than those required for LH or ICRF, and can likely accommodate a larger power density through the first wall. Examining the ITER design for equatorial launchers⁴⁴, the footprint on the first wall and subsequent volume required behind these apertures is larger than the actual exit hole for the EC beam. A placeholder value of 1 m^2 is assumed for 20 MW total power. Although this would depend on how many EC beams are accommodated, and how the beams are steered to the desired locations. In a power plant the deposition locations in the plasma region may be fixed, simplifying the EC design and minimizing the required flexibility and complexity. On the other hand, if the EC is required to provide control of neo-classical tearing modes, for example, some flexibility in steering would be required.

The reference configuration has 30 MW of ICRF at 95 MHz, and 65-80 MW of NB with 1 MeV particle energy in the flattop phase. LH can be used up to 1.0 MA, or about 30 MW) without negatively affecting the ideal stability with no wall, or higher if a wall at $b/a = 0.55$ is included. This then can reduce the power used in the NB by 20-30 MW. The electron cyclotron at the level of 20 MW is capable of modifying the q profile over $\rho = 0.2-0.6$ for control.

A number of issues persist for heating and current drive systems in the power plant fusion environment. The parts of these systems near the plasma must be made of radiation resistant materials, such as ferritic steels or tungsten, and the use of common materials like insulators, dielectrics, and copper must be minimized or eliminated. These components must also operate at high temperature since they will penetrate the blanket, and must use similar coolants as the blanket (e.g. helium). The wall-plug efficiencies associated with these various sources hovers around ~ 0.4 , since it encompasses the source efficiency, the transmission efficiency, and coupling efficiency to the plasma (for IC and LH), and can be low since incentive to improve the efficiency is a lower priority on present experiments. These structures are also mostly void, and designs that incorporate shielding need to be developed. These are essentially plasma facing components, and will see the same environment as the first wall, so that erosion, redeposition, implantation and tritium retention are all critical areas to address.

VII. The H-mode pedestal, and simple ELMs and disruption loading examination

The peeling-ballooning stability analysis from EPED1 determined the pedestal pressure height to be about 185 kPa with n_{ped} at $0.65 \times 10^{20} / \text{m}^3$. Since pedestal stored energy is defined as $3/2 p_{\text{ped}} V_{\text{plasma}}$, then $W_{\text{ped}} = 613 \text{ MJ}$, while the plasma has a total stored energy of 1530-1650 MJ (from 1.5D analysis). The plasma collisionality at the pedestal, for $T_{\text{ped}} \sim 9.0 \text{ keV}$, is ~ 0.02 , leading to a Type I ELM energy release of $\Delta W_{\text{ELM}}/\Delta W_{\text{ped}}$ of 20-25%, or 123-153 MJ. A prescription for power splits based largely on JET and ASDEX-U experiments⁴⁵⁻⁴⁷, sends 50% of the released ELM energy to the divertor, for our DN geometry we assume 65% to each divertor, and 40% of this occurs in the power rise phase, giving $\Delta W_{\text{ELM}}^{\text{div,rise}} = 16-19.9 \text{ MJ}$. The time scale based on the parallel ion front is

$\tau_{||} = 610$ microseconds. The calculated power scrape-off width from Fundamenski⁴⁸ is 3.8 mm, although the uncertainty in this parameter is large⁴⁹ and the physics is evolving. We can express our outboard divertor target area available for conducted power as

$$A_{\text{ELM,OB}} = 2\pi(R-a/2)\lambda_{\text{pow}}f_{\psi}f_{\text{tilt}}$$

which is about 2 m² assuming $f_{\psi} f_{\text{tilt}} \sim 10$. Using the semi-infinite formulation for the temperature rise at the divertor surface

$$\begin{aligned} \Delta T_{\text{rise}} (\text{°K or °C}) &= 2/3 (2 \alpha^{1/2} \Delta W_{\text{ELM}}^{\text{div,rise}}) / \\ &[\pi^{1/2} k A_{\text{ELM,OB}} (2 \tau_{||})^{1/2}], \\ &= 2/3 C_{\text{material}} \Delta W_{\text{ELM}}^{\text{div,rise}} / A_{\text{ELM,OB}} (2 \tau_{||})^{1/2} \end{aligned}$$

the temperature rise for a Type I ELM is 9545-11870 °K, leading to melting of the tungsten regardless of its operating temperature. Here we will use 3400 °C and 1500 °C for melting temperatures of tungsten and ferritic steel, respectively. There typical operating temperatures would be about 1000-1300 °C for tungsten and 550-650 °C for ferritic steel. Smaller ELM energies by a factor of at least 5 times, or a similar factor expansion of the footprint in the divertor may avoid melting, assuming an operating temperature of 1300 °C. More detailed analysis is required to model the ELM cycle with the long inter-ELM phase⁵⁰ which sets the steady temperature value of the tungsten armor, and which tend to require even larger ELM energy reductions to avoid melting. Small ELM regimes, no ELM regimes, and ELM mitigation may provide the reductions required to avoid melting, although if ELMs persist, the number of cycles experienced may be too high².

A midplane disruption (MD) is considered the worst for the up-down symmetric DN configuration. Following the same approach as in Refs. 2 and 51 for a midplane disruption, based on experimental observations⁵²⁻⁵⁴, the fraction of plasma stored energy released is 65-100%, and the time scale for this, based on the plasma volume, is about $\Delta t_{\text{TQ}} = 1.75\text{-}4.0$ ms. The plasma stored energy is ~ 1500-1650 MJ from the 1.5D simulations, so an intermediate value of 1550 MJ will be used. The MD releases all of this energy, with 10-50% going to the divertor, and the remainder assumed to go to the first wall. The area that intercepts this energy in the divertor is 5-10x the projected power scrape-off width area, and we use 20 m². The time scale for the entire disruption is ~ $4x\Delta t_{\text{TQ}}$ or about 7-16 ms. The area of the outboard first wall, since the energy loss is assumed to be entirely to the outboard for DN, is 1060 m², and with a peaking factor of 2x, the area is reduced to 530 m². Using the same semi-infinite formulation, without the 2/3 factor, since the heat load is considered sufficiently high that the entire duration ($4x\Delta t_{\text{TQ}}$) is considered, the tungsten temperature rise in the divertor would be 3800-24000 °K, leading to melting. For the first wall the temperature rise would be 720-1950 °K for tungsten, and 950-2580 °K for ferritic steel, leading to melting for the steel.

The use of disruption mitigation is to avoid the extreme heating in the divertor by radiating the plasma's stored energy to the first wall, and to suppress the formation of runaway electrons. Experiments⁵⁴⁻⁵⁸ show that about 90-100% of the plasma stored energy is radiated with massive gas injection (MGI) of noble gases (Ar, Ne) mixed with deuterium, the technique that has been studied the most. Correspondingly, the heat loads measured in the divertor are only a few percent of the plasma's stored energy. Our power plant plasma has a stored energy of 1550 MJ, and radiating this to the first wall area, with 80/20 split for the OB/IB, a peaking of 2x assumed, and over the same time scale as a thermal quench of $4 \times \Delta t_{TQ}$, we obtain a temperature rise of 1270 °K on the outboard first wall and 650 °K on the inboard inboard for tungsten. We obtain 1682 °K and 854 °K for outboard and inboard first walls, respectively, for ferritic steel. The values for tungsten are under melting, and those for ferritic steel would lead to melting. The mitigation of runaway electrons requires much larger numbers of particles input than the mitigation of the thermal quench, although these theoretical projections are uncertain and currently under investigation on experiments.

VIII. Tritium fueling, exhaust, and burnup

Based on the fusion power of 2640 MW for ACT2 there are 9.38×10^{20} DT fusion reactions/s. This is the same rate at which tritium (and deuterium) is consumed. To estimate the tritium burnup fraction we will use the helium exhaust requirement to maintain the core helium content at the levels identified in the systems code or 1.5D simulations, which is about $n_{He}/n_e \sim 10\%$. In steady state the helium exhaust rate must equal the helium production rate, where the small losses due to implanted He in the first wall structures are ignored. The exhaust rate of helium must be 9.38×10^{20} atoms/s or $11.2 \text{ Pa}\cdot\text{m}^3/\text{s}$ assuming $T_{wall} = 873 \text{ °K}$. The corresponding rate of DT exhaust based on the core plasma content is $E_{DT} = (f_{DT}/f_{He}) E_{He}$, which is $84 \text{ Pa}\cdot\text{m}^3/\text{s}$. Including the effects of helium (de-)enrichment in the divertor $\eta_{He} = (n_{He}^o/2n_{DT}^o)/(n_{He}/n_e)$, where superscript "o" refers to neutral atoms, the exhaust rate of fuel is given by $E_{DT} = (1-2f_{He}\eta_{He})/(f_{He}\eta_{He}) E_{He}$. For $\eta_{He} = 0.2$ the E_{DT} is $538 \text{ Pa}\cdot\text{m}^3/\text{s}$ for D and T atoms or $269 \text{ Pa}\cdot\text{m}^3/\text{s}$ for molecules. At a value for the enrichment of 1.0, the $E_{DT} = 89 \text{ Pa}\cdot\text{m}^3/\text{s}$ for atoms (slightly higher than estimated before since we ignore the argon impurity). The corresponding fueling rates are $F_{DT} = 291$ and $67 \text{ Pa}\cdot\text{m}^3/\text{s}$ molecules, for $\eta_{He} = 0.2$ and 1.0, respectively. The tritium burnup for these two cases are then 4% and 20%, respectively. The estimation of the tritium burnup is uncertain and discussed in more detail in ref [2].

IX. Conclusions

The ARIES-ACT2 study of a conservative physics and conservative technology power plant has identified the operating space of physics solutions with a major radius of 9.75 m, minor radius of 2.44 m, a plasma current of 14 MA, $\beta_N < 2.4$, H_{98} of 1.2-1.3, and n/n_{Gr} of 1.3. Strong plasma shaping of $\kappa_x = 2.2$, and $\delta_x = 0.625$ are used to provide a more robust operating space for fusion power production. The large plasma size is primarily driven by the simultaneous low β_N and $q_{div}^{peak} < 10 \text{ MW}/\text{m}^2$ constraints. The q_{95} of these

configurations is high at 8.0, driven by the 100% non-inductive plasma current requirement, a bootstrap fraction of 77%, and a wall-plug efficiency of 0.4 (source, transmission, and coupling). The low β_N values accessible are due to the requirement for no wall stabilization, although analysis shows that β_N values up to 2.8-3.2 could be reached with a conducting shell behind the ring structure, which is 1.35 m from the plasma outboard surface, and plasma rotation, feedback and or kinetic stabilization. The high Greenwald density ratio is driven by large plasma size, and although values like this have been obtained on tokamak experiments, the ability to provide a 100% non-inductive plasma and a detached radiating divertor (assumed in this study) under these conditions is yet to be demonstrated. The net power divided by the L to H threshold power reaches values of 1.3-1.4, which may not be consistent with the highest H-mode confinement regimes. The heating and current drive sources are ICRF/FW and NB, with the possibility of using LH to drive up to 1.0 MA with no stabilizing wall, or 1.5 MA with a stabilizing wall, to reduce the NB power and number of NB sources. The broad NB current profile is attractive for these configurations where larger total currents must be driven, since they do not strongly modify the q-profile locally. EC simulations indicate it can be used to modify the q-profile due to its flexible local deposition, but is not efficient enough for bulk CD.

Acknowledgements

We gratefully acknowledge the contribution by P. B. Snyder for the EPED1 analysis to establish the pedestal height.

This work is supported by the US DOE contract DE-AC02-76CH03073

References

1. C. E. KESSEL et al., *Fus Sci Tech*, this issue.
2. C. E. KESSEL et al, *Fus Sci Tech*, this issue.
3. R. W. CONN et al, *Nuc Fus Supplement*, **3**, 659, (1991).
4. F. NAJMABADI et al, *Nuc Fus Supplement*, **3**, 295, (1993).
5. F. NAJMABADI et al, *Fus Eng Des*, **38**, 3, (1997).
6. M. S. TILLACK et al, *Fus Eng Des*, **49-50**, 689, (2000).
7. X. R. WANG et al, *Fus Sci Tech*, **60**, 218, (2011).
8. ITER Physics Basis, Transport and Confinement, *Nucl Fusion*, **39**, 2175, (1999).
9. A. BONDESON and D. J. WARD, *Phys Rev Lett*, **72**, 2709, (1994).
10. D. J. WARD and A. BONDESON, *Phys Plasmas*, **2**, 1570, (1995).
11. A. M. GAROFALO et al, *Nucl Fusion*, **47**, 1121, (2007).
12. Y. Q. LIU et al, *Phys Plasmas*, **7**, 3681, (2000).
13. L. J. ZHENG, M. T. KOTSCHENREUTHER, and J. W. VAN DAM, *Nucl Fusion*, **49**, 075021, (2009).
14. P. B. SNYDER et al, *Nucl. Fusion*, **51**, 103016, (2011).
15. Z. DRAGOJLOVIC et al, *Fusion Eng. and Design*, **85**, 243, (2010).

16. K. KIM, et al., "A Preliminary Conceptual Design Study for Korean Fusion DEMO Reactor Magnet, " Symposium on Fusion Engineering, San Francisco, June 10-14, 2013.
17. S. C. JARDIN et al, *J. Comp. Physics*, **66**, 481, (1986).
18. W. M. TANG, *Nucl. Fusion*, **26**, 1605, (1986).
19. C. E. KESSEL et al, *Nucl. Fusion*, **47**, 1274, (2007).
20. C. ANGIONI, et al., Plasma Phys. Control. Fusion 51 (2009) 124017
21. R. HAWRYLUK, "An Empirical Approach to Tokamak Transport", Physics Close to Thermonuclear Conditions, ed. B. Coppi et al (Brussels:Commission of the European Communities), pg 19; <http://w3.pppl.gov/transp>
22. M. S. TILLACK et al, *Fus Sci Tech*, this issue.
23. Y. MARTIN et al, *J. Physics Conf. Series*, **23**, 012033, (2008).
24. M. NAGATSU et al, *J. Nuc Mat*, **220-222**, 846, (1995).
25. R. C. GRIMM et al, *J. Comp. Physics*, **49**, 94, (1983).
26. J. M. GREENE et al, *Nucl. Fusion*, **21**, 453, (1981).
27. J. DELUCIA et al, *J. Comp. Physics*, **37**, 183, (1980).
28. C. E. KESSEL et al, *Fusion Eng. Design*, **80**, 63, (2006).
29. BRAMBILLA, M., Plas Phys and Control Fusion, **41**, 1, (1999).
30. WRIGHT, J. C. et al, *Phys Plas*, **11**, 2473 (2004).
31. D. W. SWAIN and R. H. GOULDING, *Fus Engr Des*, **82**, 503, (2007).
32. R. HEMSWORTH et al, *Nuc Fus*, **49**, 045006, (2009).
33. R. J. GOLDSTON et al, *J Comp Phys*, **43**, 61, (1981).
34. D. W. IGNAT et al, *Nucl. Fusion*, **34**, 837, (1994).
35. R. W. HARVEY AND M. G. MCCOY, 1993 Proc. Of the IAEA Technical Committee on Advances in Simulation and Modeling of Thermonuclear Plasmas (Montreal, Quebec) (Vienna: IAEA) pg 489. USDOC NTIS Doc. No. DE93002962.
36. A. SMIRNOV et al, in Proceedings of the 15th Workshop on ECE and ECRH, World Scientific, 2009, p. 301.
37. P. T. BONOLI et al, Proc. 21st International Conference on Fusion Energy (Chengdu, 2006) (Vienna:IAEA) CD-ROM file PD-3 and <http://www-naweb.iaea.org/naweb/physics/FEC/FEC2006/html/index.html>.
38. P. BIBET et al, *Nucl Fusion*, **35**, 1213, (1995).
39. A. BECOULET et al, *Fusion Engr and Design*, **86**, 490, (2011).
40. J. H. BELO et al, *Nucl. Fusion*, **51**, 083017, (2011).
41. N. B. MARUSHCHENKO et al, *Phys. Plasmas*, **18**, 032501, (2011).
42. A. H. KRITZ et al, Heating in Toroidal Plasmas, Proc. 3rd Joint Varenna-Grenoble Int. Symp (Grenoble, 1982), vol 2 (Brussels, CEC), pg 707, 1982.
43. Y. R. LIN-LIU et al, *Phys. Plasmas*, **10**, 4064, (2003).
44. M. A. HENDERSON et al, *Nucl Fusion*, **48**, 054013, (2008).
45. A. LOARTE et al, *Phys Plas*, **11**, 2668, (2004).
46. T. EICH et al, *J Nuc Mat*, **415**, S856, (2011).
47. H. THOMSEN et al, *Nuc Fus*, **51**, 123001, (2011).
48. W. FUNDAMENSKI et al, *Nucl. Fusion*, **45**, 950, (2005).
49. T. EICH et al, *Nuc Fus*, **53**, 093031, (2013).
50. J. P. BLANCHARD et al, *Fus Sci Tech*, this issue.
51. C. E. KESSEL et al, *Fus Sci Tech*, accepted for publication.

52. A. LOARTE et al, "Expected Energy Fluxes onto ITER Plasma Facing Components During Disruption Thermal Quenches from Multi-Machine Data Comparisons", *Proc 20th IAEA Conf Fusion Energy*, Portugal, Nov 1-6 2004, <http://www-naweb.IAEA.org/napc/physics/fec.htm>.
53. A. LOARTE et al, *Nuc Fus*, **51**, 073004, (2011).
54. M. LEHNEN et al, *Nuc Fus*, **51**, 123010, (2011).
55. P. ANDREW et al, "Heat Load to the JET Divertor During Disruptions and Disruption Mitigation by Massive Gas Puffing", *30st EPS Conf on Contr Fus and Plasma Phys*, St. Petersburg, July 7-11 2003, vol 27A, P-1.108, ECA.
56. M. SUGIHARA et al, *Nuc Fus*, **47**, 337, (2007).
57. R. S. GRANETZ et al, *Nuc Fus*, **46**, 1001, (2006).
58. D. G. WHYTE et al, *J Nuc Mat*, **363-365**, 1160, (2007).

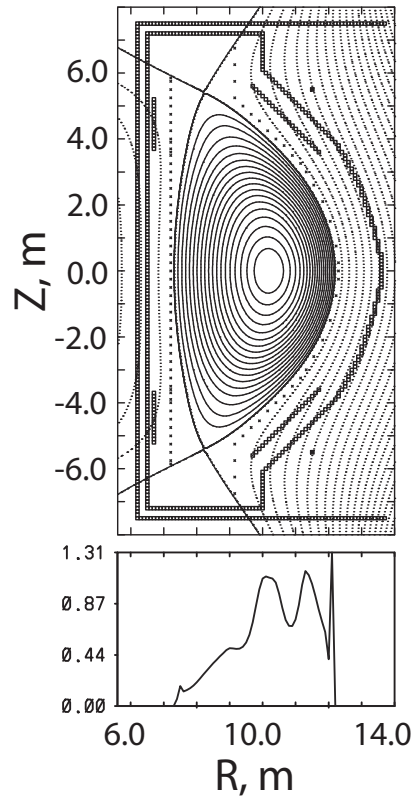


Figure 1. The poloidal cross-section of the ARIES-ACT2 plasma and dominant toroidally conducting structures, including the vacuum vessel (outermost), ring structure, and tungsten stabilizer plates (innermost), and vertical position feedback coils behind the ring structure. The plot also shows limiter points used in the TSC simulations.

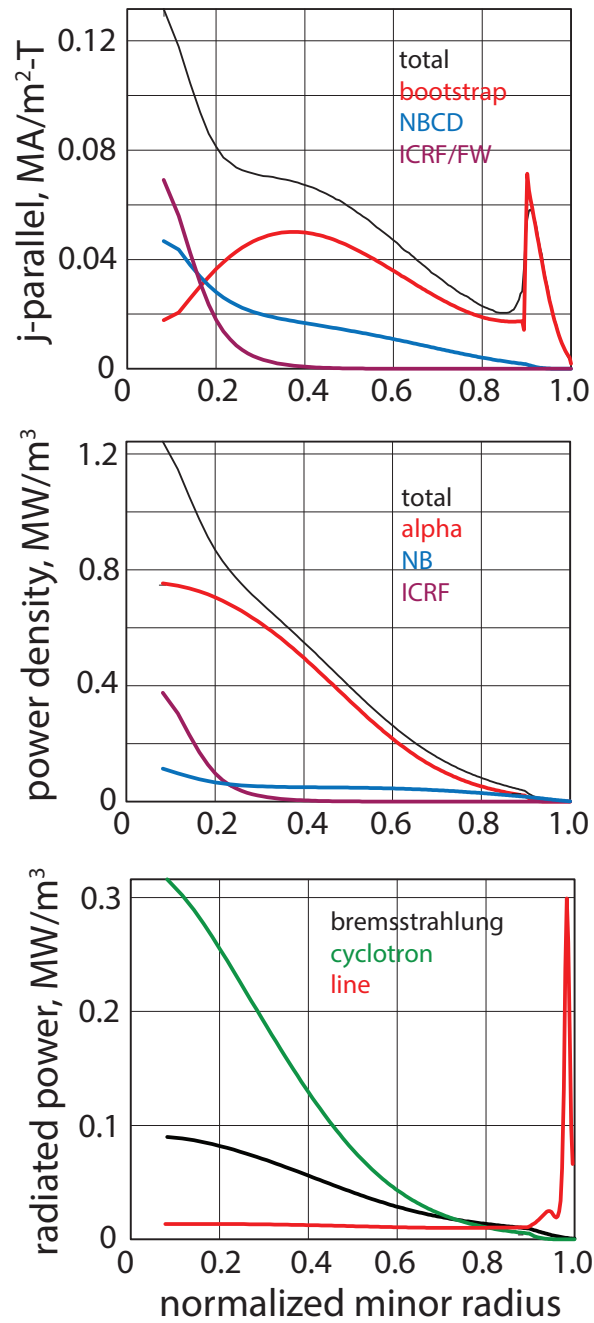


Figure 2. Profiles of the parallel current density, heating power densities, and radiation loss power densities for the broad pressure case. The heating and current drive are provided by 80 MW of NB, and 30 MW of ICRF. The large cyclotron loss power is shown.

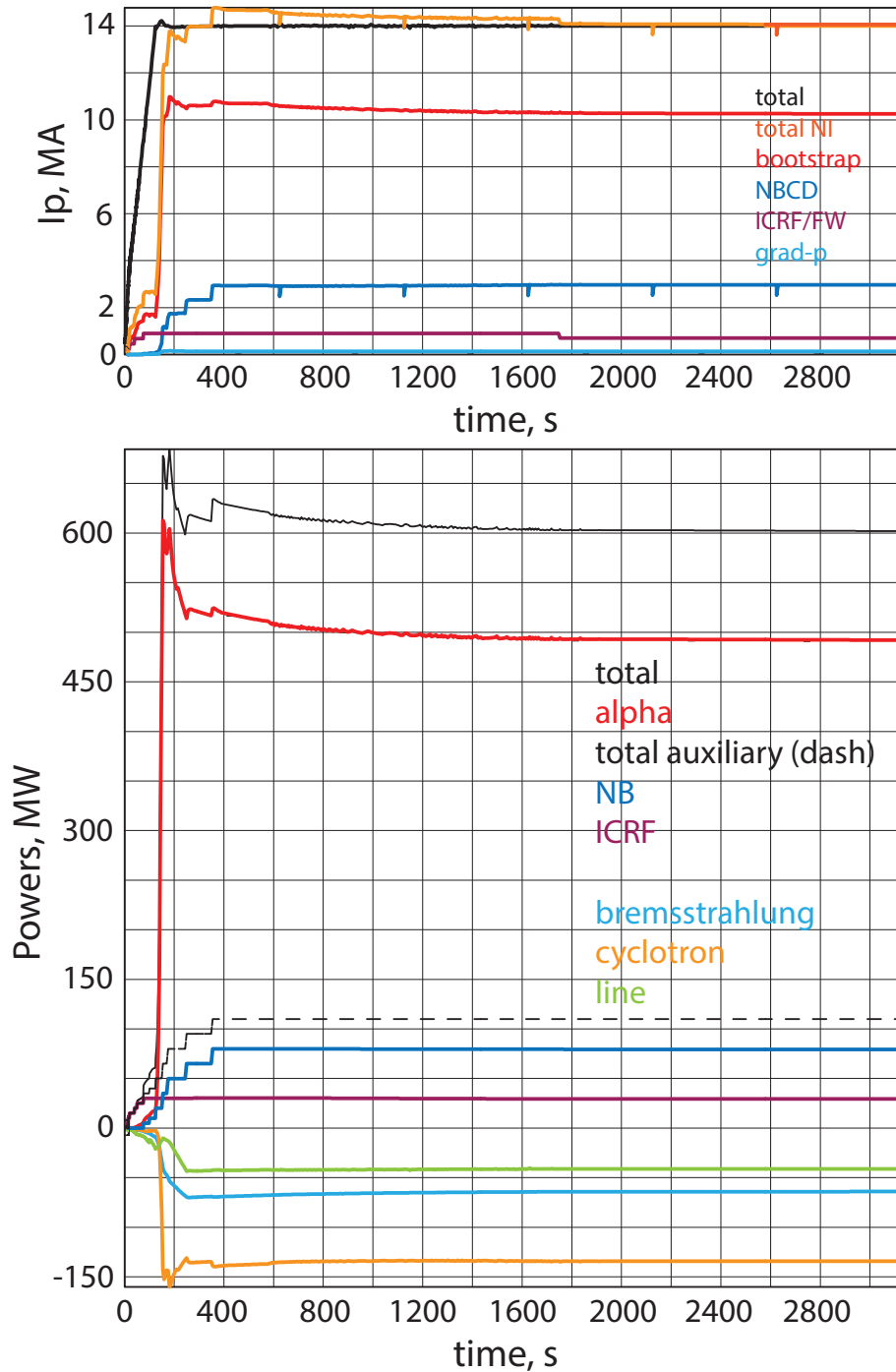


Figure 3. The time histories of the contributions to the plasma current, and input and loss powers for the broad pressure case. The NBCD and ICRF/FW provide the external current drive. The overshoot in the alpha power can be removed with improved density and power phasing.

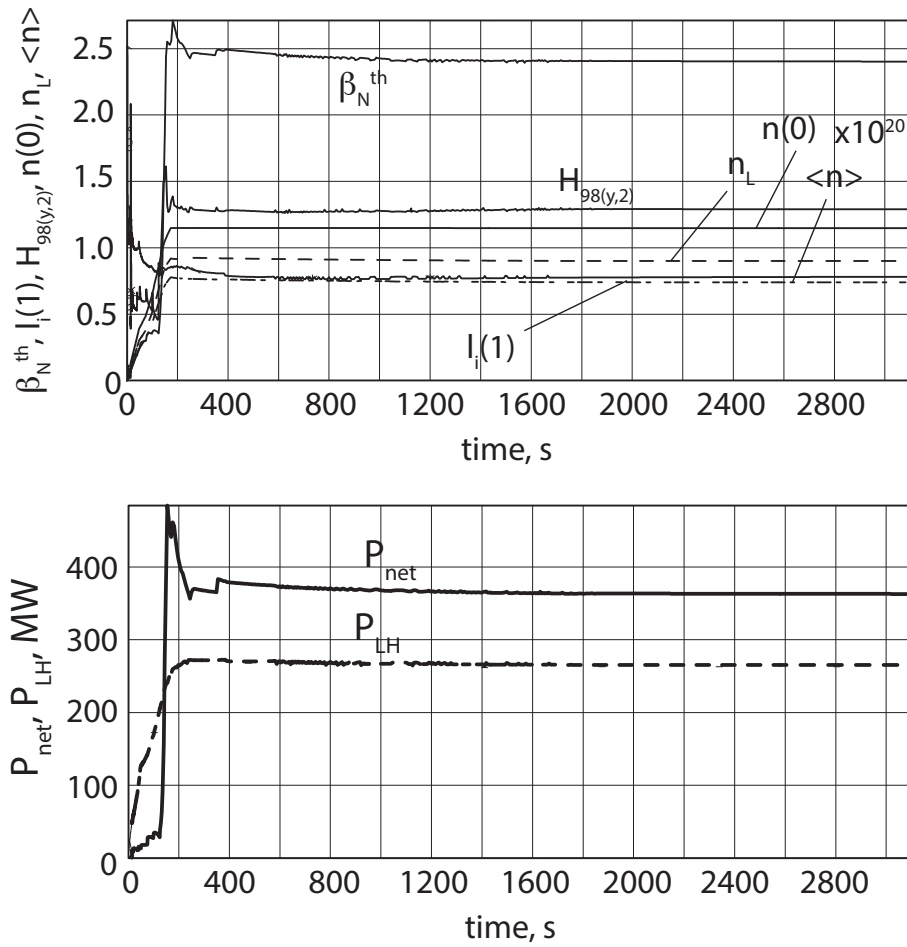


Figure 4. Time histories of the normalized beta, $H_{98(y,2)}$ global confinement multiplier, central line and volume average densities, and the $I_i(1)$, for the broad pressure case. The net power ($P_{\alpha} + P_{aux} - P_{brem} - P_{cycl} - P_{line} - dW/dt$) and the L to H threshold power are also shown, indicating a ratio in flattop of about 1.35.

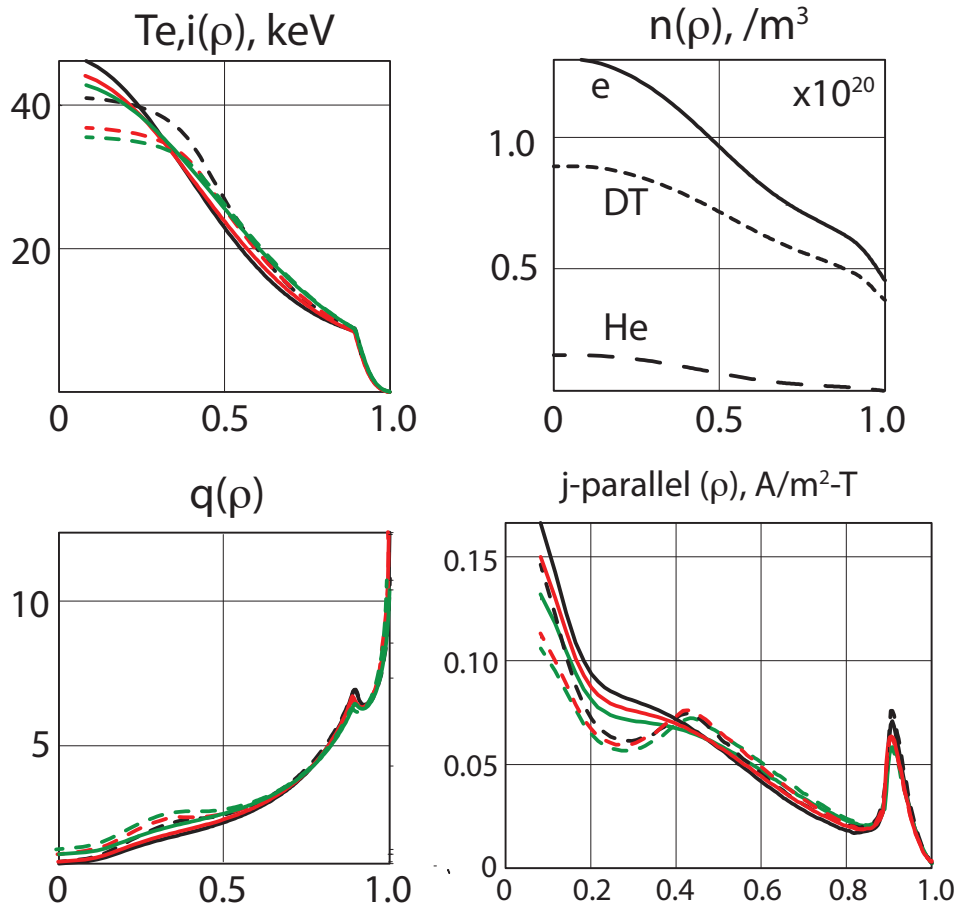


Figure 5. Profiles of the electron temperature (same as ion), densities, safety factor profiles, and parallel current densities of the 6 cases shown in Table I, broad pressure (green solid), broad pressure with flattening (green dash), medium pressure (red solid), medium pressure with flattening (red dash), peaked pressure (black solid) and peaked pressure with flattening (black dashed).

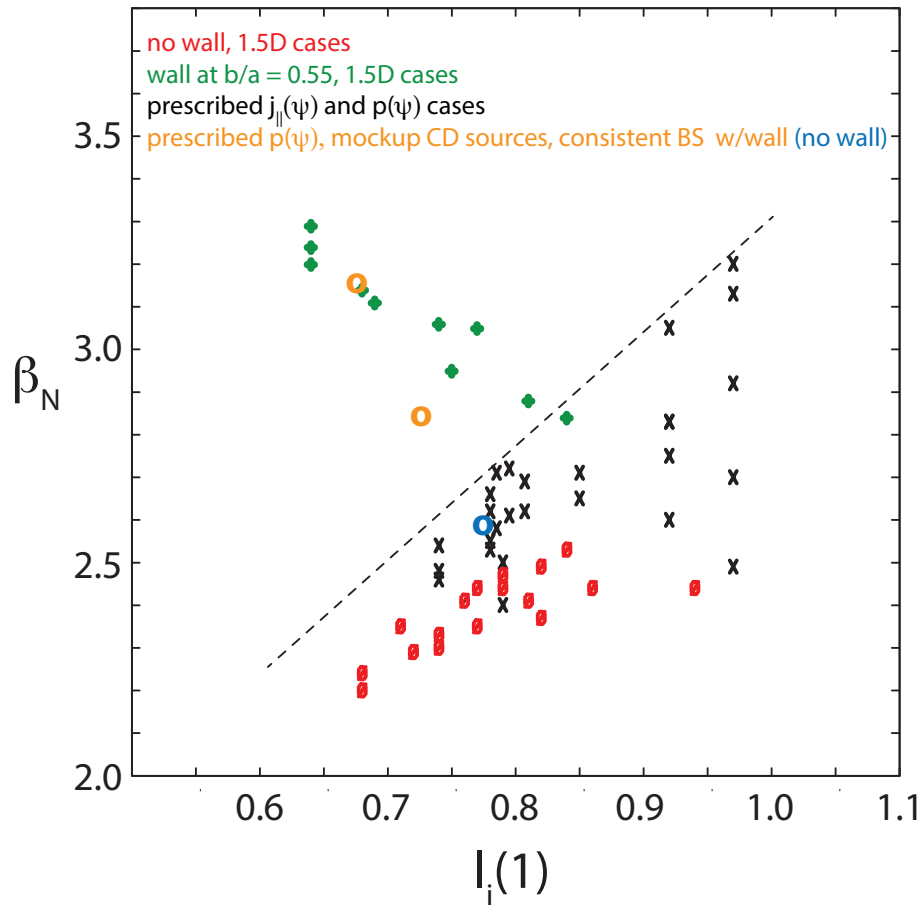


Figure 6. Ideal MHD stability for $n=1$ kink modes, showing stable cases. Initial scans prescribing j_{\parallel} and p are shown by black X's with the stable to unstable dashed line. Analysis using prescribed p and mockups of NBCD, ICRF/FW, ECCD, and LHCD are shown by open circles, blue with no wall, and orange with a wall. The 1.5D plasma configurations are shown by red, with slightly reduced pressures, and by green with slightly higher pressures and assuming a wall behind the ring structure at $b/a = 0.55$.

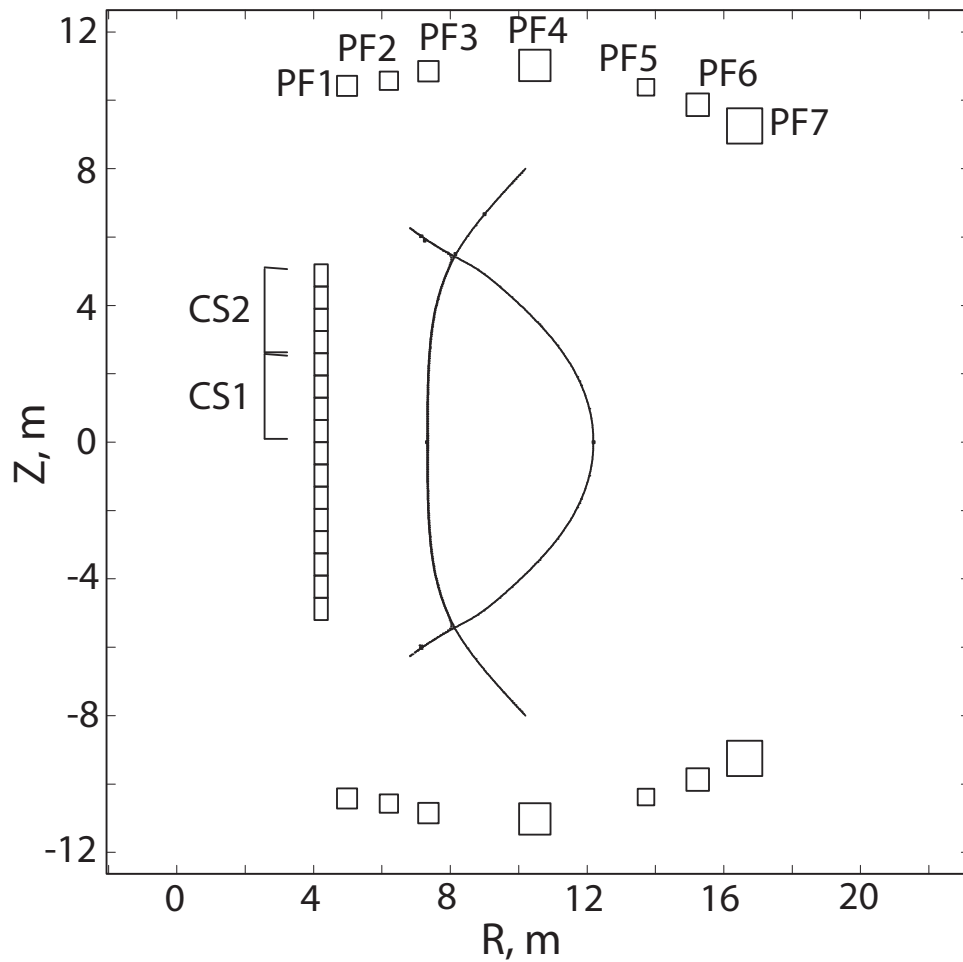


Figure 7. Layout of the final poloidal field coils and central solenoid. The locations are determined by the available space outside the TF coil support structure and the vacuum vessel port extensions.

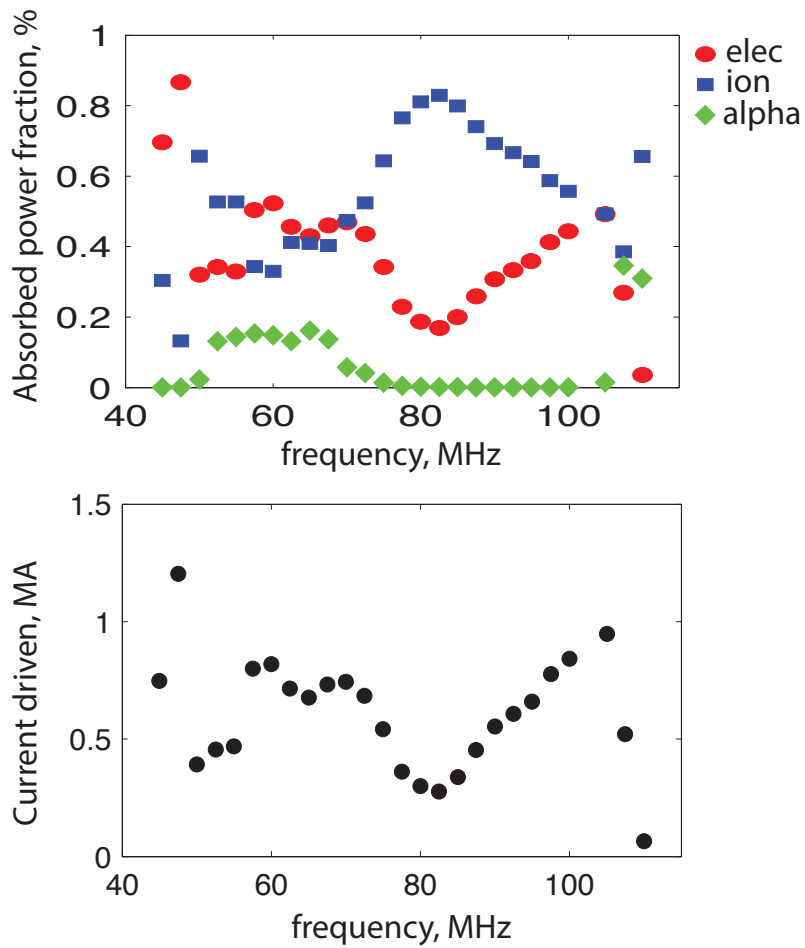


Figure 8. The ICRF absorbed power on electrons, thermal ions, and fast alphas, and the driven fast wave current, as a function of frequency. The reference frequency is chosen at 95 MHz to maximize the current drive, minimize ion absorption, and avoid impurity absorption on argon.

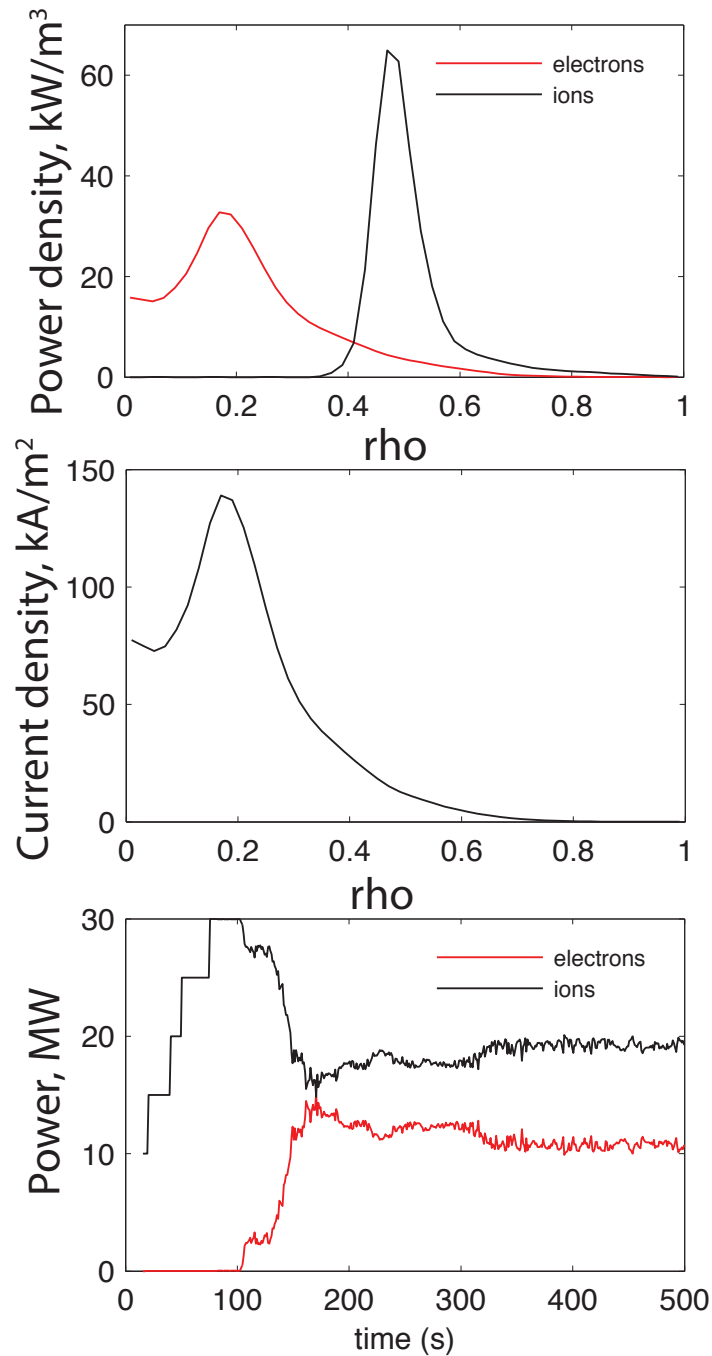


Figure 9. The deposition profiles during flattop for the power on electrons, power on thermal ions and driven fast wave current, at 95 MHz. The time histories of the power to the thermal ions and electrons, showing a delay in the electron absorption until the magnetic axis shifts with higher pressure, and the increase in the electron beta.

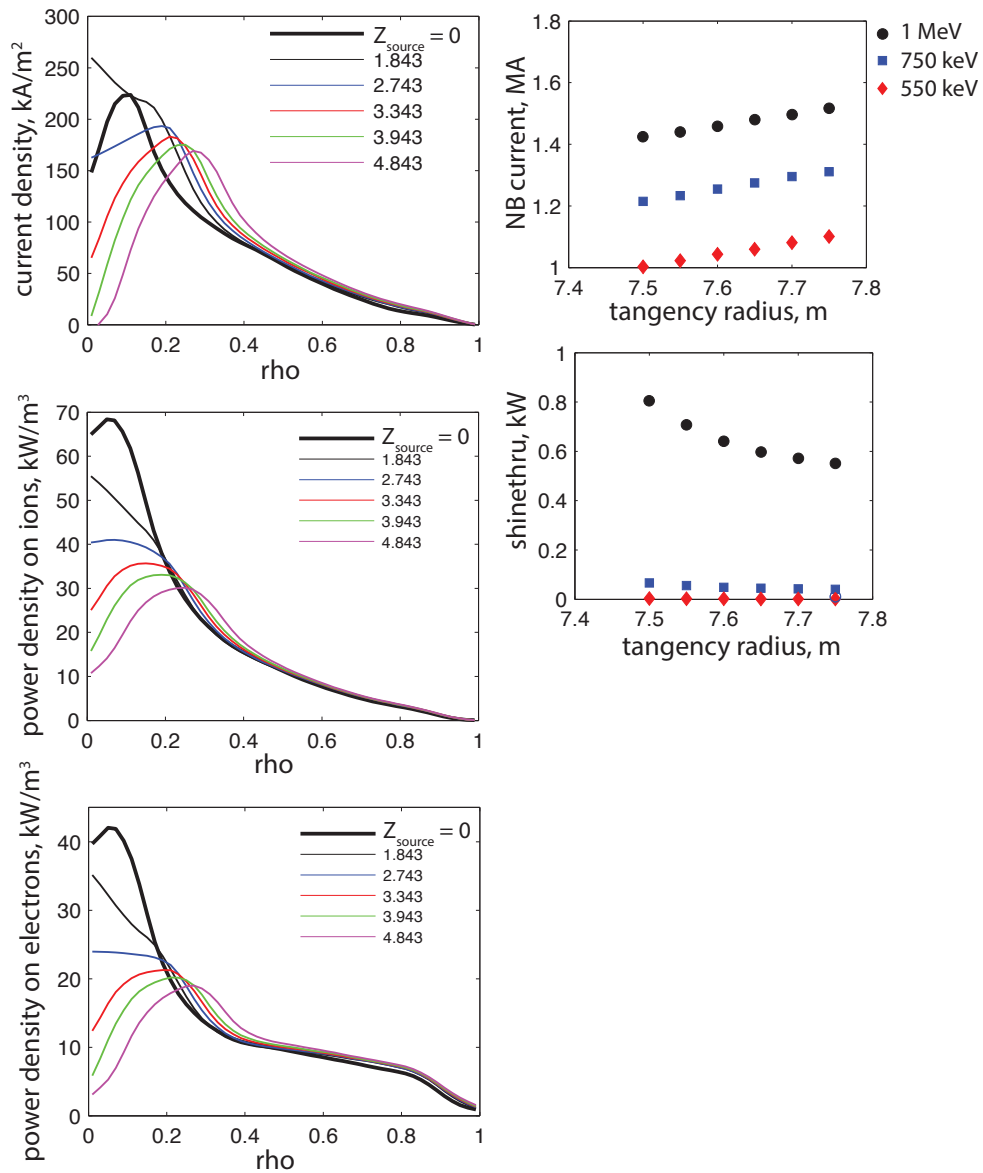


Figure 10. The neutral beam analysis results showing the current density, and power densities to electrons and ions for 1 MeV particle energy, and varying NB source height above the midplane ($Z = 0$). Also shown are the total driven current and shinethru in flattop for 1 MeV, 750 keV, and 550 keV particle energies, with source at $Z = 0$, and different tangency radii.

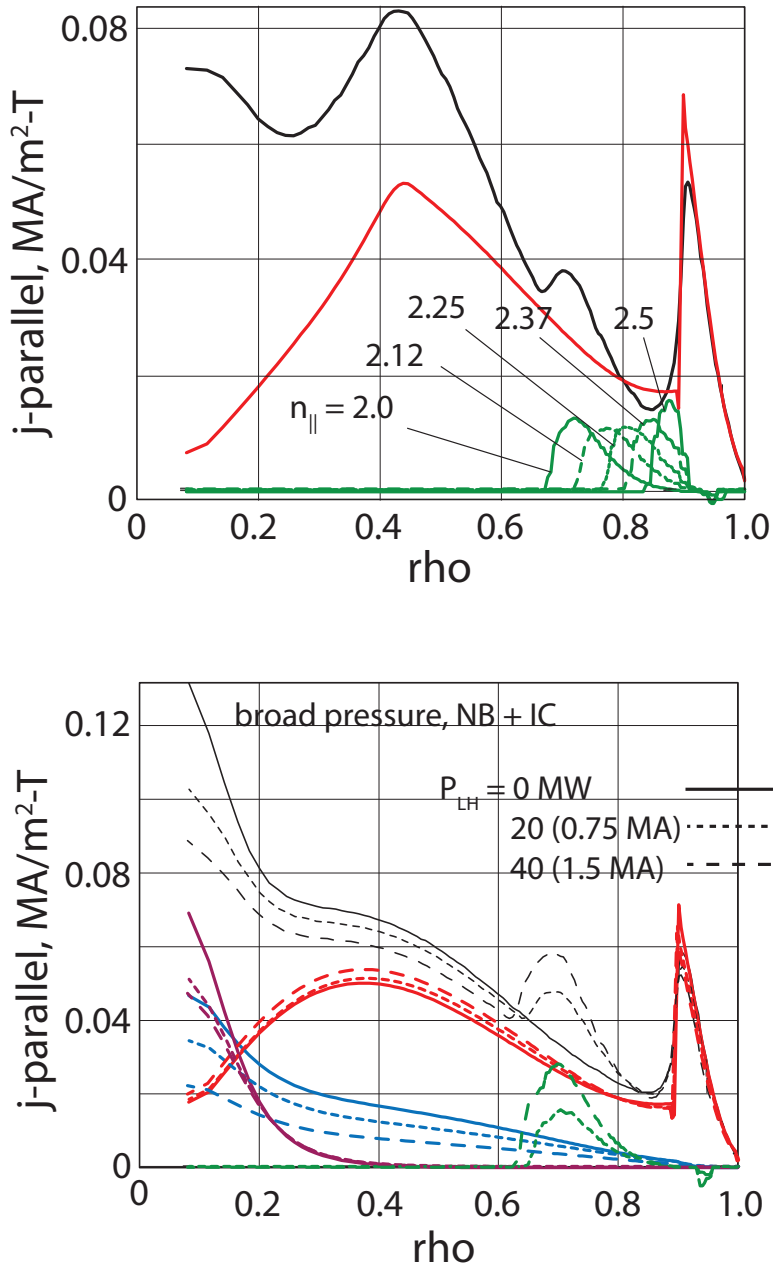


Figure 11. Parallel current density of lower hybrid waves at 5 GHz, 15 MW of LH power, and varying n_{\parallel} , showing the deposition location as the refractive index is increased. These are calculated with the broad pressure with flattening profiles. The waves are launched from the midplane (0 deg) on the outboard side. The total current and bootstrap current shown are for the $n_{\parallel} = 2.0$ case. The broad pressure case where LH is used to replace CD from the NB is shown for 20 and 40 MW of LH power, with $n_{\parallel} = 2.0$, and are compared to the case with no LH, indicating the reduction in the on-axis current density.

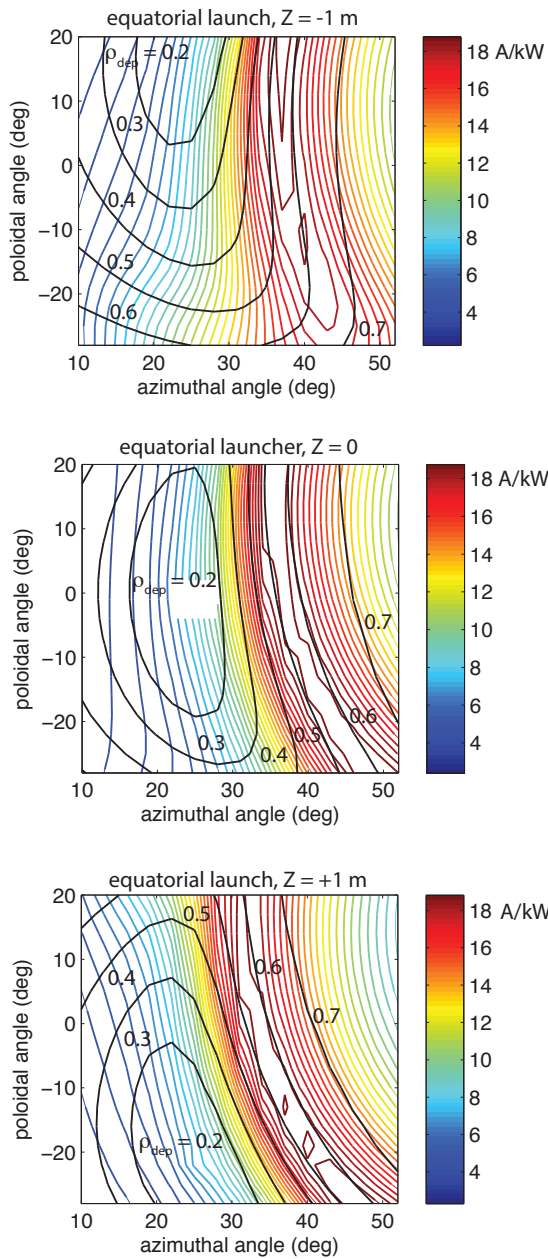


Figure 12. Scans of the poloidal and toroidal steering angles for EC from the equatorial launcher at $Z = 0, +1$ m, and -1 m. The deposition locations are shown by black contours, and the color-coded contours provide the resulting current drive efficiency. These launcher locations provide the highest current and largest deposition flexibility. Higher frequency can improve the current drive efficiency.

The Princeton Plasma Physics Laboratory is operated
by Princeton University under contract
with the U.S. Department of Energy.

Information Services
Princeton Plasma Physics Laboratory
P.O. Box 451
Princeton, NJ 08543

Phone: 609-243-2245
Fax: 609-243-2751
e-mail: pppl_info@pppl.gov
Internet Address: <http://www.pppl.gov>